bioRχiv

Developmental dynamics and axonal transport of cerebral cortex projection neuron mRNAs *in vivo*

Priya Veeraraghavan[a,*], Dustin E. Tillman[a,*], Melody I. Ross[a], and Jeffrey D. Macklis[a,#]
[a]Department of Stem Cell and Regenerative Biology, and Center for Brain Science, Harvard University, Cambridge, MA, USA
*These authors contributed equally to this work
[#]Correspondence should be addressed to J.D.M. (jeffrey_macklis@harvard.edu)

Appropriate development of long-range nervous system circuitry requires dynamic regulation of subcellular mRNA localization, but little is known about how specific neuron subtypes control this critical process *in vivo*. Here, we employ an integrated genetic and temporally controlled approach to investigate *in vivo* developmental mRNA dynamics in somata and axons of a prototypical cerebral cortex projection neuron subtype, callosal projection neurons (CPN), which connect the cortical hemispheres to integrate sensorimotor information, and regulate high-level associative cognition and behavior. We identify cis-regulatory elements that are associated with mRNA turnover in CPN somata, including specific 3' untranslated regions (UTRs), and elucidate distinct modes of axon transport in CPN axons for function-specific mRNA classes. Together, these findings elucidate how developing CPN control subcellular mRNA localization, and how dysregulation of these processes might lead to neurodevelopmental and/or neurodegenerative disorders. More broadly, this work identifies general mRNA localization mechanisms that likely function across projection neuron subtypes, and in other polarized cells.

Introduction

During development, projection neurons of the cerebral cortex (in particular, the evolutionarily recent neocortex) construct specific circuits by extending long axons (hundreds to thousands of cell body (soma) diameters long in mouse; longer in developing humans) to precisely innervate distant targets[1]. Growth cones (GCs) are subcellular structures at leading edges of each axon that regulate this navigation via integration of complex extracellular cues into directional responses, before ultimately maturing into presynapses[2]. To effect appropriate growth and guidance, axons and GCs dynamically regulate local proteomes that are distinct from their parent somata[3,4]. This differential subcellular localization is established both by direct trafficking of proteins, and by local translation of specific mRNAs after selective stabilization, export, and transport from somata to axons and GCs[5,6]. Extremely polarized cortical projection neurons must precisely control subcellar mRNA localization, and are particularly susceptible to dysregulation of these processes, which can result in neurodevelopmental and neurodegenerative diseases[7].

Intracellular mRNA gradients are present in neurons[8-11], glia[12], oocytes[13-16], yeast[17], and even leading edges of migrating fibroblasts[18]. Differential mRNA densities are established by a suite of RNA binding proteins (RBPs) that associate in *trans* with individual mRNAs, then direct their transport to subcellular compartments, and/or modulate their local stability[19]. RBP-mRNA interactions are driven by cis-regulatory sequences or structural elements in each individual mRNA, frequently in 3' untranslated regions (UTRs)[20], as well as by local concentrations of RBPs, many of which competitively bind to the same mRNA element[21].

Several approaches enable isolation of mRNAs with cell-type and/or subcellular specificity *in vivo*. For example, translating ribosome affinity purification (TRAP) identifies actively translated mRNAs from complex tissue via genetically encoded ribosomal tags[22]. To identify mRNAs that are actively being translated, our lab recently developed experimental and analytical approaches to identify transcriptomes of subtype-specific GCs and their parent somata directly from specific neuron subtypes *in vivo* via subcellular biochemical fractionation and fluorescent small particle sorting (FSPS)[23,24]. This work has identified that GC transcriptomes are strikingly different from those of their parent somata[23], are selectively dysregulated by deletion of key transcription factors[25,26], are distinct across neuron subtypes and developmental stages[27], and produce GC-localized proteins that regulate subtype-specific circuit formation[23,28]. However, mRNA subcellular localization is dynamically regulated, involving transport, stabilization, and degradation, and these approaches only enable steady-state investigation of transcriptomes and translatomes.

Dynamic regulation of mRNA stability has been studied via approaches that either induce a rapid change in transcription[29], or introduce a non-native, chemically distinct nucleotide metabolite into newly transcribed mRNA[30-33]. Chemicals that inhibit transcription (e.g. alpha-amanitin, actinomycin D, 5,6-dichloro-1-beta-ribo-furanosyl benzimidazole (DRB)) cause widespread transcriptional arrest that alters RNA degradation kinetics[34,35], and cannot be used *in vivo*. Temporally resolved *in vivo* metabolic labeling of neuronal projection mRNAs has only been performed in retinal ganglion cells[36], in which partial cell-type specificity was achieved via injection into a specific tissue (e.g. the eye).

Here, we employ a combined genetic and temporally controlled approach to investigate developmental mRNA dynamics in somata and projections of callosal projection neurons (CPN), the projection neuron subtype that connects the cortical hemispheres, and plays key roles in high-level integrative, associative, cognitive, and behavioral functions[37]. We express uracil phosphoribosyltransferase (UPRT), which catalyzes the conversion of uracil to uridine, specifically in CPN, then systemically administer 4-thiouracil (4TU), leading to selective incorporation of 4-thiouridine

(4sU) into CPN mRNAs. 4sU-containing mRNAs are detected via a nucleotide conversion approach[30,38], combined with computational modeling and inference[39,40], enabling identification of newly transcribed CPN mRNAs in both somata and axons, estimations of mRNA turnover, and functions of 3' UTRs in regulating mRNA stability.

We identify *cis*-regulatory features in CPN mRNAs that are correlated with mRNA half-life in somata, and likely regulate transcript turnover; these include AU-rich elements, distinct RBPs, and GC localization. We also identify stabilizing/sequestering UTRs via a luciferase reporter assay, and detect distinct classes of mRNAs in CPN axons across developmental times and subcellular compartments, suggesting axonal transport mechanisms that are specific for distinct functional classes of mRNAs.

These insights into developmental mRNA dynamics of cerebral cortex projection neurons (CPN in particular) *in vivo*, combined with the experimental and analytical approaches that we develop, and partially described in dissertation work from our lab[41], will enable future elucidation of molecular mechanisms regulating appropriate and/or aberrant mRNA stability and transport in CPN, in distinct projection neuron subtypes, and in other polarized cells.

Results

Time- and subtype-specific metabolic labeling *in vivo*

To identify newly synthesized transcripts in a specific projection neuron subtype with temporal resolution in vivo, we adapted metabolic labeling approaches for use in callosal projection neurons (CPN). Briefly, we introduced plasmids to CPN that encode for TdTomato and *T. gondii* uracil phosphoribosyltransferase (UPRT) via *in utero* electroporation (IUE) at embryonic day (E) 14.5 (Figures 1A-B). We then administered 4-thiouracil (4TU, 450 mg/kg) to pups at postnatal day (P) 2 or 3; 4TU is converted into 4-thiouridine (4sU) by UPRT, and incorporated into newly transcribed mRNAs[42]. We purified CPN somata with subtype specificity via fluorescence-activated cell sorting (FACS) 2, 4, 6, or 8 hours after 4TU administration, extracted RNA, and identified newly synthesized transcripts via T->C conversions, using SLAM-seq and 3 'end sequencing[30]. As expected, the labeling rate increases over time post-injection, and is significantly higher in UPRT-containing CPN compared to TdTomato-only CPN (Figure 1C); these control CPN display some background labeling from low activity of endogenous *M. musculus* UPRT[43]. Subcutaneous injection of 4TU led to robust labelling with minimal background, while intraperitoneal (IP) injection led to higher labeling in both background and experimental samples (Figure S1A), likely due to greater bioavailability of 4TU[44]. Therefore, subcutaneous injections were used for soma samples, and IP injections were used for lower-input axon samples (discussed below).

We next investigated kinetics of individual mRNAs in CPN somata by estimating new transcript ratios (NTRs) for each transcript with a Poisson mixture model approach, using bakR[40] (Figures 1D, S1B-E). We model relative mRNA half-lives ($t_{1/2}$) by fitting NTRs to a model of first-order exponential decay, as previously described[39,40]. Importantly, pulse labeling of 4TU/4sU *in vivo* leads to a decrease in global labeling rate over time (Figure S1F), in contrast to constant *in vitro* labeling rates, so we scaled NTRs by a

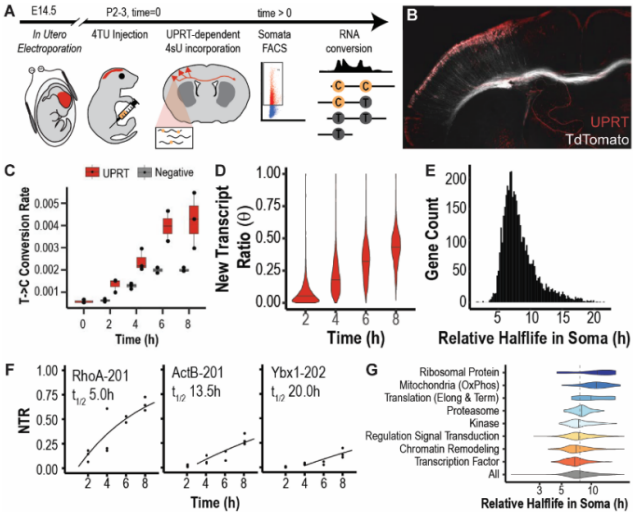

Figure 1: Temporally resolved, subtype-specific metabolic labeling of CPN mRNAs *in vivo*. (A) Schematic for metabolic labeling of CPN transcripts *in vivo*. CPN express fluorophore and UPRT via E14.5 IUE. At P2 or P3 (t = 0), 4TU is administered via intraperitoneal injection, then fluorescent CPN somata are purified at distinct time points via FACS for RNA extraction, sequencing, and conversion quantification. **(B)** CPN labeled via E14.5 IUE express myristoylated TdTomato (white) and UPRT (red). **(C)** T->C conversion rate increases over time post-injection, and it is significantly higher in samples with UPRT. **(D)** Mean new transcript ratio (NTR) per gene increases over time post-injection. **(E)** Distribution of transcript relative half-lives in CPN somata (RH_{soma}). **(F)** Changes in NTR over time, and RH_{soma} estimates for exemplar mRNAs with turnover that is fast (RhoA), medium (ActB), and slow (Ybx1). Points are per-sample maximum likelihood NTR estimates. Line is predicted curve. **(G)** RH_{soma} distributions are distinct across mRNAs associated with distinct functional gene ontology (GO) terms.

global scaling factor to account for this decrease in label (Figures S1G-I). Resulting CPN soma $t_{1/2}$ ranged from 1.5 hours to 21.4 hours, with a mean of 7.6 hours (Figure 1E).

NTRs increase when new mRNA is introduced to the system (e.g. via transcription), and/or when old mRNA is removed (e.g. via degradation). We identify that per-gene transcription rates are relatively constant over the investigated time course (Figure S1J), so changes in NTR are primarily driven by removal of old transcripts. In most cells, from which the whole volume is sampled via sequencing, this removal is primarily or entirely due to degradation of old mRNAs. However, CPN, and the broad class of projection neurons, are highly polarized, so old RNA is removed from somata both by decay, and transport to subcellular compartments, particularly axons and GCs (Figure 2A). Therefore, we define the "relative half-life of a transcript" (RH) for each distinct subcompartment (e.g. RH_{soma}).

To cross-check our estimated CPN RH_{soma} values, we compared our findings to previous work in other systems[10,30,31,45-59]. Notably, per-gene RH_{soma} values are correlated across these distinct experimental contexts, indicating broad conservation of mRNA stability mechanisms, and are most highly correlated with primary cortical neurons *in vitro*[57] (Spearman rho=0.63, Figure S1K), which most closely resemble CPN *in vivo*. Importantly, exemplar transcripts that are quickly degraded (e.g. RhoA[60]), or highly stable (e.g. Ybx1[61]), demonstrate appropriate kinetics (Figure 1F), as do gene sets defined by gene ontology (GO) terms[62,63] – mRNAs encoding for proteins that function in translation and mitochondria have longer RH_{soma} values, while RH_{soma}

values are shorter for mRNAs encoding transcription factors and chromatin remodelers[56] (Figure 1G).

RH_{soma} is linked with stability, degradation, and transport

Since 3' untranslated regions (UTRs) regulate key aspects of mRNA stability and localization[20], we next investigated whether *cis*-regulatory structures and sequence features correlate with RH_{soma} by evenly dividing transcripts into 5 bins based on RH_{soma} (Figure 2B). As predicted, UTR length only weakly correlates with RH_{soma}, most notably with the slowest turnover mRNAs having the shortest UTRs (Figure S2A). This weak correlation is expected, since additional sequence elements can be either stabilizing or degrading[20].

In contrast, 3' UTR nucleotide content correlates with RH_{soma}, with A, T, and AT-rich 3' UTRs having shorter RH_{soma}, while C and GC-rich 3' UTRs have longer RH_{soma} (Figure 2C). To determine if this correlation is caused by AU-rich elements (AREs), known to enhance mRNA degradation[64], we scored sequences with AREscore[65], which assesses ARE likelihood based on the number of observed motifs and their proximity to each other. Consistent with prior work, we identify that higher AREscore values are associated with shorter RH_{soma} (Figure 2D), indicating conservation of a key mRNA degradation mechanism in developing CPN.

3' UTRs are typically bound by RNA binding proteins (RBPs) for additional regulation of mRNA stability and localization[20], so we next investigated whether RBP-specific sequence features correlate with RH_{soma}. Intriguingly, 3' UTR minimum free energy of folding (MFE), calculated by Vienna RNAFold[66], then normalized for length and GC content, is lower for mRNAs with shorter RH_{soma} (Figures 2E, S2B), indicating that high-turnover transcripts have more secondary structure, and likely more RBP binding[67].

To identify RBPs that potentially regulate mRNA stability, degradation, and/or transport, we investigated enrichment of RBP binding sites in 3' UTRs across RH_{soma}. Strikingly, mRNAs with long RH_{soma} are overrepresented for motifs bound by Pcbp and Rbfox family members, known mRNA stabilizers[68,69], as well as other RBP motifs (Figure 2F). In contrast, Rbms1 binding sites are enriched in mRNAs with short RH_{soma}, suggesting that Rbms1 might destabilize these transcripts, and/or transport them to CPN axons and GCs during development, as we recently reported[27].

Rbms1 binds to AU repeats[70], which localize mRNAs to neuronal projections[71]. Therefore, we investigated associations between RH_{soma} values and 3' UTR AU repeats, and other potential indicators of axonal transport. We identify that RH_{soma} values are negatively correlated with lengths of the longest AU repeat (Figure 2G), but only 15% of these regions are likely AREs (Figure S2C), indicating that this effect is independent of ARE-mediated destabilization (Figure 2D). Further, mRNAs with long (> 8 nt) AU repeats are enriched for GO terms associated with axons and synapses (Figure 2H), and 3' UTRs with AU repeats have greater evolutionary conservation (Figures S2D). These results indicate that AU repeats in 3' UTRs likely target mRNAs to CPN axons and GCs in development, potentially via Rbms1. Indeed, mRNAs with short RH_{soma} values (and long AU repeats) are enriched for mRNAs that we identified as GC-localized in developing CPN during active axon elongation[27] (Figure 2I).

3 'UTRs of Gpm6a and Gnas stabilize and sequester mRNAs

Next, we directly investigated potential functions of specific 3' UTRs in regulating mRNA stability, degradation, and/or transport by developing and employing an *in vivo* inducible luciferase library assay. Briefly, we introduce into CPN plasmids that encode mClover and a synthetically designed library of doxycycline-dependent *R. reniformis* luciferases, each of which is fused to a distinct 3' UTR, via E14.5 IUE (Figure 3A). We administered doxycycline (100 mg/kg) to pups at P2 or P3 via intraperitoneal injection to produce a pulse of luciferase expression, purified CPN somata via FACS 3 or 8 hours after injection, extracted RNA, and quantified UTR-specific changes in luciferase abundance via 3' amplicon sequencing.

To identify UTRs with distinct roles in mRNA dynamics, we investigated 3' UTRs from Gad1 and Ldlrad3, which we recently identified as GC- and soma-localizing[27], respectively, and 6 UTRs that span a range of RH_{soma} (Figure 3B): Auts2 (5.6 h); Marcks

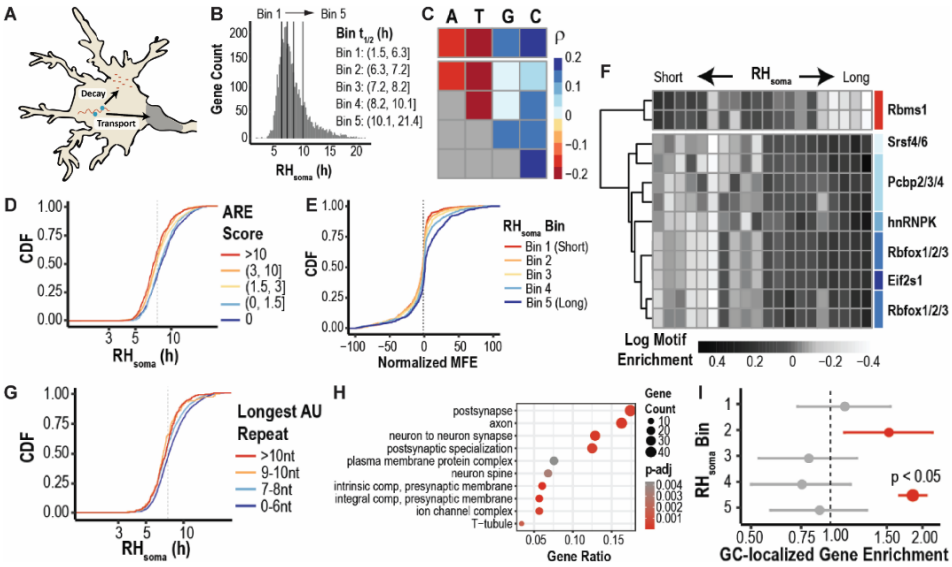

Figure 2: *Cis*-regulatory 3' UTR sequence features are associated with CPN RH_{soma}. (A) Schematic highlighting how short RH_{soma} can result from mRNA degradation and/or transport to axons/GCs. **(B)** Equal division of CPN mRNAs into five bins, based on RH_{soma}. **(C)** Single- (top row) and di- (matrix) nucleotide frequencies correlate with RH_{soma}. Spearman correlation coefficient. **(D)** High likelihood AU-rich elements (AREs) are negatively associated with RH_{soma}. **(E)** Normalized minimum free energy of folding (MFE) is positively associated with RH_{soma}. **(F)** Enrichment for RNA binding protein (RBP) motifs in 3' untranslated regions (UTRs), based on RH_{soma}. All motifs have a linear relationship between RH_{soma} and motif enrichment, with consistency between data and a fitted linear model, as measured by an F-test (adjusted p-value < 0.05). **(G)** Length of the longest AU repeat in a 3' UTR is negatively associated with RH_{soma}. **(H)** mRNAs with a longest AU repeat longer than 8 nt are enriched for synapse and axon GO terms (FDR < 0.05). **(I)** mRNAs with short RH_{soma} are GC-localized in developing CPN, as recently identified by our group[27].

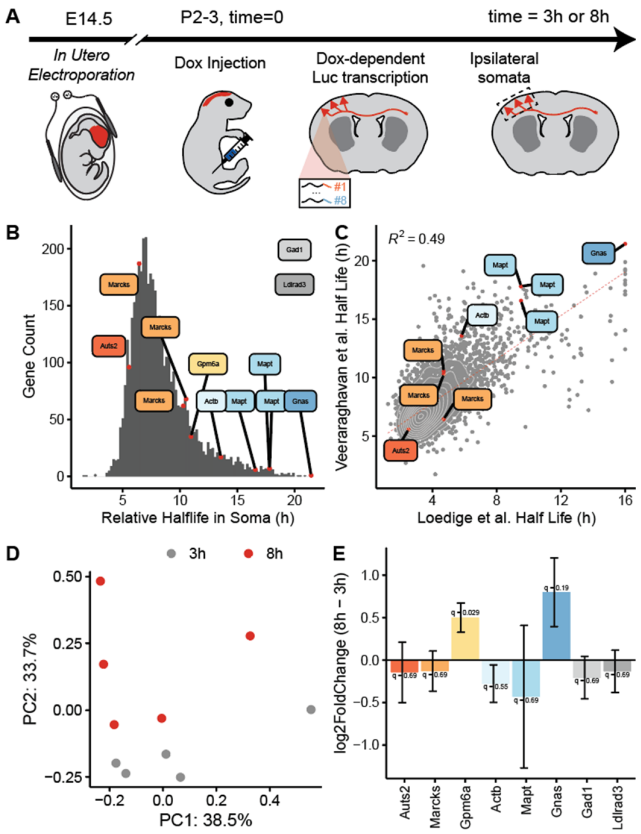

Figure 3: Identification of 3' UTRs regulating mRNA dynamics in developing CPN. (A) Schematic for *in vivo* inducible luciferase library assay in CPN. CPN express fluorophore and a library of doxycycline-dependent luciferases, each of which is fused to a distinct 3' UTR, via E14.5 IUE. At P2/P3 (t = 0), doxycycline is injected into intraperitoneal cavity, then CPN somata are fluorescently purified at distinct times via FACS for RNA extraction, sequencing, and differential expression analysis. **(B)** 3' UTRs are associated with localization to cell bodies (Ldlrad3), GCs (Gad1), or span a range of RH_{soma}. **(C)** 3' UTRs have similar RH_{soma} in primary cultured cortical neurons. **(D)** Time-matched samples cluster via principal component analysis (PCA). **(E)** Luciferases fused to 3' UTRs from Gpm6a or Gnas significantly increase over time.

(6.4 – 10.5 h); Gpm6a (11.0 h); Actb (13.6 h); Mapt (16.6 – 17.8 h); and Gnas (21.4 h). Importantly, these UTRs have similar RH_{soma} in primary cultured neurons from cortex[57] (Figure 3C), increasing confidence that *in vivo* functions of these UTRs are conserved in CPN.

As predicted, all barcodes are identified with high confidence by thousands of unique molecular identifiers (UMIs; Figures S3A-B), and time-matched samples cluster via principal component analysis (PCA; Figure 3D). Importantly, library and mClover UMIs increase over time (Figure S3C), and are linearly correlated (Figure S3D), so we normalized each UTR UMI count by both factors prior to differential expression analysis via DESeq2[72].

Strikingly, 3' UTRs of Gpm6a and Gnas lead to a significant increase in luciferase mRNA over time (Figure 3E), suggesting that these motifs stabilize CPN mRNAs, and/or sequester them from axons and GCs. We attempted to investigate functions of 3' UTRs in subcellular targeting by repeating this experiment with extraction of mRNA from microdissected CPN axons, rather than from purified CPN somata (Figure S3E). However, few UMIs were identified (Figures S3F-G), potentially due to insufficient CPN axon enrichment,

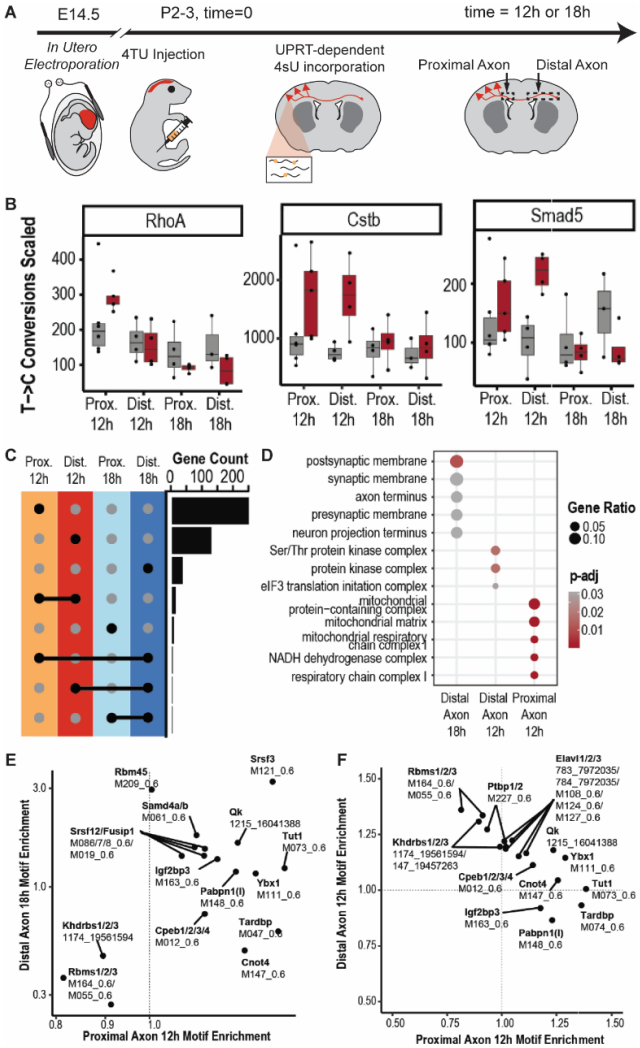

Figure 4: Identification of mRNAs in CPN axons across spatial and temporal domains. (A) Schematic for metabolic labeling of CPN axonal mRNAs *in vivo*. **(B)** Identification of exemplar genes in CPN axons that have been previously identified to localize to, and/or be locally translated in, axons (RhoA, Cstb, Smad5), as demonstrated by significant T->C conversions over background. **(C)** Labeled axonal gene sets are distinct across temporal and spatial domains. **(D)** Labeled axonal gene sets are enriched for distinct GO terms across temporal and spatial domains. **(E, F)** Labeled axonal gene sets are enriched for distinct RBP binding motifs across temporal and spatial domains.

bottlenecking of mRNAs in somata, and/or poor overlap between CPN labeling and doxycycline exposure. This negative result further motivated our investigations of *in vivo* CPN axon mRNA dynamics via metabolic labeling.

Identification of mRNAs transported to CPN axons

To identify CPN mRNAs that are subcellularly localized *in vivo*, we adapted our metabolic labeling approaches for axons. Briefly, we introduced plasmids to CPN that encode for TdTomato and UPRT via E14.5 IUE, administered 4TU to pups at P2 or P3, and extracted RNA from microdissected axons 12 or 18 hours after 4TU administration that are either pre-midline ("proximal"), or post-midline ("distal"), for SLAM-Seq[30] (Figures 4A, S4A-B). Critically, we account for variable IUE efficiencies by quantifying relative levels of reporter mRNAs fused to an ActB axonal trafficking zipcode via qPCR[73] (Figure S4C), and by quantifying TdTomato

abundance via western blot after normalization by the axonal protein Ncam[74] (Figure S4D). We then estimate enrichment of conversions in UPRT samples with a negative binomial generalized linear model (GLM), and identify significantly labeled transcripts via a one-sided Wald test (FDR < 0.2; Figures S4E-J). As predicted, we identify transcripts in CPN axons that others have described as localizing to, and/or being locally translated in, axons and GCs (e.g. RhoA[75], Cstb[76], Smad5[77]; Figure 4B).

Strikingly, labeled gene sets have minimal overlap across axon regions and time points (Figure 4C), and distinct GO terms are overrepresented in each gene set (Figure 4D), suggesting distinct mechanisms regulating function-specific mRNA transport. Further, these gene sets have differences in RH_{soma} (Figure S4K), 3 UTR length (Figure 4SL), and RBP binding sequences (Figures 4E-F). In particular, mRNAs in distal axons 12 hours after 4TU administration, the most rapidly transported mRNAs, are overrepresented for AU- and A-rich motifs that are bound by Rbms and Khdrbs RBP families, while these sequences are depleted in all other gene sets. Intriguingly, this group of mRNAs also has longer AU repeats in their 3 UTRs (Figure S4L), which are located closer to their coding sequences (CDS; Figure S4M), and include axon-localized mRNAs Cstb[76] and Smad5[77], as well as Efr3a, which previously has been identified to regulate CPN radial migration via Rbms1 binding[78]. Together, these results both identify *in vivo* CPN mRNAs in axons and indicate distinct RBP-mediated transcript transport mechanisms based on functional protein class.

Discussion

Dynamics and transport of CPN mRNAs *in vivo*

In this work, we develop an approach for subtype-specific, *in vivo* metabolic labeling of newly transcribed mRNAs with temporal resolution, enabling developmental investigation of mRNA dynamics and subcellular localization, as well as molecular mechanisms regulating these critical processes. We employ cerebral cortex callosal projection neurons (CPN) as a prototypical highly polarized neuron subtype. In particular, we quantify *in vivo* mRNA half-lives in CPN somata (RH_{soma}), and validate our estimates via comparison to exemplar transcripts, previously identified dynamics of gene classes, and *in vitro* work by others (Figures 1, S1). We also identify cis-regulatory features in 3 'untranslated regions (UTRs) that regulate mRNA dynamics in developing CPN, including nucleotide content, motifs for distinct RNA binding proteins (RBPs), and signatures of soma export (Figures 2, S2). We identify that 3 'UTRs of Gpm6a and Gnas confer stability, and/or sequester mRNAs from axons, in CPN by employing an *in vivo* luciferase library reporter assay (Figures 3, S3). Finally, we adapt our subtype-specific, *in vivo* metabolic labeling approach for distinct subcellular compartments by integrating proximal and distal axon microdissection, and identify dynamic mRNA subcellular localization across temporal and spatial domains, indicating distinct, function-specific mechanisms regulating mRNA transport (Figures 4, S4).

Overall, this work demonstrates that this newly developed approach for *in vivo* metabolic labeling with subtype and subcellular specificity enables developmental identification of mRNA stability and localization, and elucidation of molecular mechanisms regulating these key processes, which are strikingly dysfunctional across a range of neurodevelopmental and neurodegenerative diseases.

3 UTR AU repeats regulate mRNA stability and transport

We identify that AU-rich sequences are associated with fast mRNA turnover in CPN somata, and, for a subset of genes with this motif, with efficient transport to axons. Both phenomena have been previously described, with AU-rich elements (AREs) making mRNAs more sensitive to degradation[79,80], and AU repeats designating mRNAs for transport to axons[81]. However, little is known about how these processes are regulated by distinct RBPs.

Intriguingly, we identify that binding sites for Rbms1, a known regulator of CPN mRNA stability via AU repeat binding[78], and a regulator of CPN circuit formation[27], are enriched among mRNAs with short RH_{soma}, and among mRNAs that are rapidly trafficked to CPN axons, suggesting that Rbms1 binding at AU repeats might regulate mRNA export from CPN somata. We attempted to test this hypothesis directly via knockdown of Rbms1 in CPN, followed by RNA-seq. However, this manipulation both increased CPN death and dysregulated CPN migration to layer II/III, preventing transcriptomic investigation. Future work would be enabled by development of new approaches for precise temporal specificity over Rbms1 manipulation to further understand its function(s) in CPN development.

Elavl RBPs, highly abundant in CPN somata[27] and promoters of CPN subtype identity[82], also bind AU-rich sequences, and are overrepresented among RBP binding sites in rapidly trafficked axonal mRNAs, suggesting potential function in mRNA export from CPN somata. Future work could deepen understanding of how such RBPs distinguish AREs and AU repeats from AU-rich sequences in bound RNAs for degradation and transport, respectively.

CPN employ function-specific modes of axonal transport

We identify distinct modes of function-specific mRNA transport in CPN via the unbiased and high-throughput approaches employed here for *in vivo* metabolic labeling with temporal and subcellular resolution. For example, mitochondrial genes are overrepresented among mRNAs that slowly traffick to CPN axons, and granules with these mRNAs are enriched on Rab7a+ late endosomes, which pause in proximity to mitochondria and likely serve as translation platforms[83], indicating a slow, organelle-based mechanism of mRNA transport. In contrast, mRNAs encoding for kinases and synaptic machinery are more rapidly transported to axons. Since rates of net anterograde axon transport are inversely proportional to granule size[83], these mRNAs, and other mRNAs with AU-rich motifs, are likely transported at low copy numbers, possibly with even a single mRNA per granule.

3 'UTRs of Gnas and Gpm6a confer mRNA stability in CPN

We identify specific roles of distinct 3 'UTRs in regulating CPN mRNA dynamics *in vivo* by developing and employing a luciferase construct library. In particular, we find that the 3 'UTR of Gnas, which encodes for a G_s alpha subunit that activates intracellular signaling pathways downstream of G protein-coupled receptors (GPCRs)[84], and that has a quite long RH_{soma}, causes luciferase mRNA to be significantly

stabilized and/or sequestered from axons, directly linking this sequence to CPN mRNA dynamics. Further, we identify that the 3 'UTR of Gpm6a, which encodes a neuronal membrane glycoprotein[85], also stabilizes luciferase mRNA in CPN somata. We and others have demonstrated that Gpm6a mRNA is abundant in axons and neurites[23,27,57], and that this transcript has a long half-life in neurites[57]. These results indicate that an axon-permissive signal is encoded either in full-length Gpm6a mRNA or by a factor that is introduced in *trans* co-transcriptionally.

Rbfox proteins regulate developmental mRNA dynamics

We identify several features associated with enhanced CPN mRNA stability *in vivo*, including a lack of mRNA structure, consistent with previous reports that mRNA secondary structure leads to degradation[86]. Strikingly, binding motifs of many RBPs are enriched among low turnover mRNAs, especially those of the Rbfox family, suggesting RBP-mediated control over mRNA stability. Although Rbfox proteins are primarily known for regulating nuclear pre-mRNA splicing[87], a cytoplasmic Rbfox1 isoform binds 3 ' UTRs of synaptic mRNAs associated with autism spectrum disorders (ASDs), stabilizing them by blocking miRNA binding[69]. Together, these results indicate that Rbfox1 regulates cytosolic mRNA developmental dynamics in CPN, likely via stabilization of select mRNAs.

New approaches for *in vivo* metabolic labeling of neurons

We identify newly transcribed CPN mRNAs *in vivo* by developing and employing cell-type specific metabolic labeling approaches with temporal and subcellular resolution. Despite the success of these approaches, several opportunities for improvement remain. Boosting signal is a persistent problem *in vivo*, particularly in the central nervous system (CNS), where the blood brain barrier (BBB) blocks most systemically delivered molecules, including uracil analogs[38,88]. One possible solution is pretreatment of mice with 5-eniluracil (5EU), which inhibits the first step of uracil catabolism, potentially leading to more sustained 4TU circulation, as previously described for the chemotherapeutic agent 5-fluorouracil (5FU)[89]. Reducing background labeling is also challenging, since nucleotide scavenging pathways and endogenous UPRT paralogs prevent total noise elimination[43]. However, several groups have jointly engineered UPRT enzyme and uracil analogs to enable efficient uracil conversion with minimal endogenous scavenging. In particular, a rationally designed UPRT, combined with 5-vinyluracil (5VU), is a promising approach[33,88].

Conclusion

Overall, the work reported here establishes a set of experimental and analytical approaches to investigate *in vivo* mRNA dynamics of subtype-specific projection neurons with temporal and subcellular resolution. We identify developmental regulators of mRNA stability and axonal transport, enabling future studies of how these mechanisms regulate mRNA trafficking during development and in mature circuits, and how perturbation of these processes might contribute to neurodevelopmental and neurodegenerative diseases. Importantly, these approaches generalize to other neuron types, polarized cells, and/or tissues, substantially enabling and expanding investigation of *in vivo* mRNA dynamics across diverse systems and disorders.

References

1. Greig, L. C., Woodworth, M. B., Galazo, M. J., Padmanabhan, H. & Macklis, J. D. Molecular logic of neocortical projection neuron specification, development and diversity. Nat Rev Neurosci 14, 755-769 (2013). https://doi.org/10.1038/nrn3586
2. Lowery, L. A. & Van Vactor, D. The trip of the tip: understanding the growth cone machinery. Nat Rev Mol Cell Biol 10, 332-343 (2009). https://doi.org/10.1038/nrm2679
3. Campbell, D. S. & Holt, C. E. Chemotropic responses of retinal growth cones mediated by rapid local protein synthesis and degradation. Neuron 32, 1013-1026 (2001). https://doi.org/10.1016/s0896-6273(01)00551-7
4. Cagnetta, R., Frese, C. K., Shigeoka, T., Krijgsveld, J. & Holt, C. E. Rapid Cue-Specific Remodeling of the Nascent Axonal Proteome. Neuron 99, 29-46 e24 (2018). https://doi.org/10.1016/j.neuron.2018.06.004
5. Rotem, N. et al. ALS Along the Axons - Expression of Coding and Noncoding RNA Differs in Axons of ALS models. Sci Rep 7, 44500 (2017). https://doi.org/10.1038/srep44500
6. Zappulo, A. et al. RNA localization is a key determinant of neurite-enriched proteome. Nat Commun 8, 583 (2017). https://doi.org/10.1038/s41467-017-00690-6
7. Prashad, S. & Gopal, P. P. RNA-binding proteins in neurological development and disease. RNA Biol 18, 972-987 (2021). https://doi.org/10.1080/15476286.2020.1809186
8. Bassell, G. J. et al. Sorting of β-Actin mRNA and Protein to Neurites and Growth Cones in Culture. The Journal of Neuroscience 18, 251-265 (1998). https://doi.org/10.1523/jneurosci.18-01-00251.1998
9. Taliaferro, J. M. et al. Distal Alternative Last Exons Localize mRNAs to Neural Projections. Mol Cell 61, 821-833 (2016). https://doi.org/10.1016/j.molcel.2016.01.020
10. Tushev, G. et al. Alternative 3' UTRs Modify the Localization, Regulatory Potential, Stability, and Plasticity of mRNAs in Neuronal Compartments. Neuron 98, 495-511.e496 (2018). https://doi.org/10.1016/j.neuron.2018.03.030
11. Gumy, L. F. et al. Transcriptome analysis of embryonic and adult sensory axons reveals changes in mRNA repertoire localization. Rna 17, 85-98 (2011). https://doi.org/10.1261/rna.2386111
12. Yergert, K. M., Doll, C. A., O'Rouke, R., Hines, J. H. & Appel, B. Identification of 3' UTR motifs required for mRNA localization to myelin sheaths in vivo. PLoS Biol 19, e3001053 (2021). https://doi.org/10.1371/journal.pbio.3001053
13. Cote, C. A. et al. A Xenopus protein related to hnRNP I has a role in cytoplasmic RNA localization. Mol Cell 4, 431-437 (1999). https://doi.org/10.1016/s1097-2765(00)80345-7
14. Hartswood, E., Brodie, J., Vendra, G., Davis, I. & Finnegan, D. J. RNA:RNA interaction can enhance RNA localization in Drosophila oocytes. Rna 18, 729-737 (2012). https://doi.org/10.1261/rna.026674.111
15. Kim-Ha, J., Smith, J. L. & Macdonald, P. M. oskar mRNA is localized to the posterior pole of the Drosophila oocyte. Cell 66, 23-35 (1991). https://doi.org/10.1016/0092-8674(91)90136-m
16. Neuman-Silberberg, F. S. & Schüpbach, T. The Drosophila dorsoventral patterning gene gurken produces a dorsally localized RNA and encodes a TGF alpha-like protein. Cell 75, 165-174 (1993).
17. Bobola, N., Jansen, R. P., Shin, T. H. & Nasmyth, K. Asymmetric accumulation of Ash1p in postanaphase nuclei depends on a myosin and restricts yeast mating-type switching to mother cells. Cell 84, 699-709 (1996). https://doi.org/10.1016/s0092-8674(00)81048-x
18. Dermit, M. et al. Subcellular mRNA Localization Regulates Ribosome Biogenesis in Migrating Cells. Dev Cell 55, 298-313.e210 (2020). https://doi.org/10.1016/j.devcel.2020.10.006
19. Gerstberger, S., Hafner, M. & Tuschl, T. A census of human RNA-binding proteins. Nat Rev Genet 15, 829-845 (2014). https://doi.org/10.1038/nrg3813
20. Mayr, C. What Are 3' UTRs Doing? Cold Spring Harb Perspect Biol 11 (2019). https://doi.org/10.1101/cshperspect.a034728
21. Gardiner, A. S., Twiss, J. L. & Perrone-Bizzozero, N. I. Competing Interactions of RNA-Binding Proteins, MicroRNAs, and Their Targets Control Neuronal Development and Function. Biomolecules 5, 2903-2918 (2015). https://doi.org/10.3390/biom5042903
22. Shigeoka, T. et al. Dynamic Axonal Translation in Developing and Mature Visual Circuits. Cell 166, 181-192 (2016). https://doi.org/10.1016/j.cell.2016.05.029

23. Poulopoulos, A. et al. Subcellular transcriptomes and proteomes of developing axon projections in the cerebral cortex. Nature 565, 356-360 (2019). https://doi.org/10.1038/s41586-018-0847-y
24. Engmann, A. K. et al. Neuronal subtype-specific growth cone and soma purification from mammalian CNS via fractionation and fluorescent sorting for subcellular analyses and spatial mapping of local transcriptomes and proteomes. Nat Protoc 17, 222-251 (2022). https://doi.org/10.1038/s41596-021-00638-7
25. Durak, O. et al. ASD gene Bcl11a regulates subcellular RNA localization, associative circuitry, and social behavior. bioRxiv (2022).
26. Itoh, Y. et al. Bcl11b orchestrates subcerebral projection neuron axon development via cell-autonomous, non-cell-autonomous, and subcellular mechanisms. bioRxiv (2024).
27. Veeraraghavan, P. et al. Dynamic subtype- and context-specific subcellular RNA regulation in growth cones of developing neurons of the cerebral cortex. bioRxiv (2024).
28. Poulopoulos, A. et al. Symmetry in levels of axon-axon homophilic adhesion establishes topography in the corpus callosum and development of connectivity between brain hemispheres. bioRxiv (2024).
29. Harrold, S., Genovese, C., Kobrin, B., Morrison, S. L. & Milcarek, C. A comparison of apparent mRNA half-life using kinetic labeling techniques vs decay following administration of transcriptional inhibitors. Anal Biochem 198, 19-29 (1991). https://doi.org/10.1016/0003-2697(91)90500-s
30. Herzog, V. A. et al. Thiol-linked alkylation of RNA to assess expression dynamics. Nat Methods 14, 1198-1204 (2017). https://doi.org/10.1038/nmeth.4435
31. Schofield, J. A., Duffy, E. E., Kiefer, L., Sullivan, M. C. & Simon, M. D. TimeLapse-seq: adding a temporal dimension to RNA sequencing through nucleoside recoding. Nature methods 15, 221-225 (2018). https://doi.org/10.1038/nmeth.4582
32. Jao, C. Y. & Salic, A. Exploring RNA transcription and turnover in vivo by using click chemistry. Proc Natl Acad Sci U S A 105, 15779-15784 (2008). https://doi.org/10.1073/pnas.0808480105
33. Nguyen, K. et al. A Bump-Hole Strategy for Increased Stringency of Cell-Specific Metabolic Labeling of RNA. ACS Chem Biol 15, 3099-3105 (2020). https://doi.org/10.1021/acschembio.0c00755
34. Chen, C. Y., Xu, N. & Shyu, A. B. mRNA decay mediated by two distinct AU-rich elements from c-fos and granulocyte-macrophage colony-stimulating factor transcripts: different deadenylation kinetics and uncoupling from translation. Mol Cell Biol 15, 5777-5788 (1995). https://doi.org/10.1128/mcb.15.10.5777
35. Chen, C. Y., Ezzeddine, N. & Shyu, A. B. Messenger RNA half-life measurements in mammalian cells. Methods Enzymol 448, 335-357 (2008). https://doi.org/10.1016/s0076-6879(08)02617-7
36. Jung, J. et al. mRNA transport, translation, and decay in adult mammalian central nervous system axons. Neuron (Cambridge, Mass.) 111, 650-668.e654 (2023). https://doi.org/10.1016/j.neuron.2022.12.015
37. Fame, R. M., MacDonald, J. L. & Macklis, J. D. Development, specification, and diversity of callosal projection neurons. Trends Neurosci 34, 41-50 (2011). https://doi.org/10.1016/j.tins.2010.10.002
38. Matsushima, W. et al. SLAM-ITseq: sequencing cell type-specific transcriptomes without cell sorting. Development 145, dev164640 (2018). https://doi.org/10.1242/dev.164640
39. Jürges, C., Dölken, L. & Erhard, F. Dissecting newly transcribed and old RNA using GRAND-SLAM. Bioinformatics 34, i218-i226 (2018). https://doi.org/10.1093/bioinformatics/bty256
40. Vock, I. W. & Simon, M. D. bakR: uncovering differential RNA synthesis and degradation kinetics transcriptome-wide with Bayesian hierarchical modeling. Rna 29, 958-976 (2023). https://doi.org/10.1261/rna.079451.122
41. Veeraraghavan, P. Subtype- and Context-Dependent Subcellular mRNA Regulation in Axons and Growth Cones of Neocortical Projection Neurons. (Harvard University, 2023).
42. Miller, M. R., Robinson, K. J., Cleary, M. D. & Doe, C. Q. TU-tagging: cell type-specific RNA isolation from intact complex tissues. Nat Methods 6, 439-441 (2009). https://doi.org/10.1038/nmeth.1329
43. Ghosh, A. C., Shimell, M., Leof, E. R., Haley, M. J. & O'Connor, M. B. UPRT, a suicide-gene therapy candidate in higher eukaryotes, is required for Drosophila larval growth and normal adult lifespan. Sci Rep 5, 13176 (2015). https://doi.org/10.1038/srep13176
44. Al Shoyaib, A., Archie, S. R. & Karamyan, V. T. Intraperitoneal Route of Drug Administration: Should it Be Used in Experimental Animal Studies? Pharm Res 37, 12 (2019). https://doi.org/10.1007/s11095-019-2745-x
45. Agarwal, V. & Kelley, D. R. The genetic and biochemical determinants of mRNA degradation rates in mammals. Genome Biol 23, 245 (2022). https://doi.org/10.1186/s13059-022-02811-x
46. Geula, S. et al. Stem cells. m6A mRNA methylation facilitates resolution of naïve pluripotency toward differentiation. Science 347, 1002-1006 (2015). https://doi.org/10.1126/science.1261417
47. Rabani, M. et al. Metabolic labeling of RNA uncovers principles of RNA production and degradation dynamics in mammalian cells. Nat Biotechnol 29, 436-442 (2011). https://doi.org/10.1038/nbt.1861
48. Spies, N., Burge, C. B. & Bartel, D. P. 3' UTR-isoform choice has limited influence on the stability and translational efficiency of most mRNAs in mouse fibroblasts. Genome Res 23, 2078-2090 (2013). https://doi.org/10.1101/gr.156919.113
49. Eisen, T. J. et al. The Dynamics of Cytoplasmic mRNA Metabolism. Mol Cell 77, 786-799.e710 (2020). https://doi.org/10.1016/j.molcel.2019.12.005
50. Erhard, F. et al. scSLAM-seq reveals core features of transcription dynamics in single cells. Nature 571, 419-423 (2019). https://doi.org/10.1038/s41586-019-1369-y
51. Tani, H. et al. Genome-wide determination of RNA stability reveals hundreds of short-lived noncoding transcripts in mammals. Genome Res 22, 947-956 (2012). https://doi.org/10.1101/gr.130559.111
52. Ke, S. et al. m(6)A mRNA modifications are deposited in nascent pre-mRNA and are not required for splicing but do specify cytoplasmic turnover. Genes Dev 31, 990-1006 (2017). https://doi.org/10.1101/gad.301036.117
53. Zheng, X. et al. CNOT3-Dependent mRNA Deadenylation Safeguards the Pluripotent State. Stem Cell Reports 7, 897-910 (2016). https://doi.org/10.1016/j.stemcr.2016.09.007
54. Sharova, L. V. et al. Database for mRNA half-life of 19 977 genes obtained by DNA microarray analysis of pluripotent and differentiating mouse embryonic stem cells. DNA Res 16, 45-58 (2009). https://doi.org/10.1093/dnares/dsn030
55. Friedel, C. C., Dölken, L., Ruzsics, Z., Koszinowski, U. H. & Zimmer, R. Conserved principles of mammalian transcriptional regulation revealed by RNA half-life. Nucleic Acids Res 37, e115 (2009). https://doi.org/10.1093/nar/gkp542
56. Schwanhäusser, B. et al. Global quantification of mammalian gene expression control. Nature 473, 337-342 (2011). https://doi.org/10.1038/nature10098
57. Loedige, I. et al. mRNA stability and m6A are major determinants of subcellular mRNA localization in neurons. Molecular Cell (2023). https://doi.org/https://doi.org/10.1016/j.molcel.2023.06.021
58. Lee, J. E., Lee, J. Y., Wilusz, J., Tian, B. & Wilusz, C. J. Systematic analysis of cis-elements in unstable mRNAs demonstrates that CUGBP1 is a key regulator of mRNA decay in muscle cells. PLoS One 5, e11201 (2010). https://doi.org/10.1371/journal.pone.0011201
59. Lugowski, A., Nicholson, B. & Rissland, O. S. DRUID: a pipeline for transcriptome-wide measurements of mRNA stability. Rna 24, 623-632 (2018). https://doi.org/10.1261/rna.062877.117
60. Xing, L., Yao, X., Williams, K. R. & Bassell, G. J. Negative regulation of RhoA translation and signaling by hnRNP-Q1 affects cellular morphogenesis. Mol Biol Cell 23, 1500-1509 (2012). https://doi.org/10.1091/mbc.E11-10-0867
61. Evdokimova, V. et al. The major mRNA-associated protein YB-1 is a potent 5' cap-dependent mRNA stabilizer. EMBO J 20, 5491-5502 (2001). https://doi.org/10.1093/emboj/20.19.5491
62. Ashburner, M. et al. Gene ontology: tool for the unification of biology. The Gene Ontology Consortium. Nat Genet 25, 25-29 (2000). https://doi.org/10.1038/75556
63. Gene Ontology, C. et al. The Gene Ontology knowledgebase in 2023. Genetics 224 (2023). https://doi.org/10.1093/genetics/iyad031
64. Barreau, C., Paillard, L. & Osborne, H. B. AU-rich elements and associated factors: are there unifying principles? Nucleic Acids Res 33, 7138-7150 (2005). https://doi.org/10.1093/nar/gki1012
65. Spasic, M. et al. Genome-Wide Assessment of AU-Rich Elements by the AREScore Algorithm. PLOS Genetics 8, e1002433 (2012). https://doi.org/10.1371/journal.pgen.1002433
66. Lorenz, R. et al. ViennaRNA Package 2.0. Algorithms Mol Biol 6, 26 (2011). https://doi.org/10.1186/1748-7188-6-26
67. Oikonomou, P., Goodarzi, H. & Tavazoie, S. Systematic identification of regulatory elements in conserved 3' UTRs of human transcripts.

Cell Rep 7, 281-292 (2014). https://doi.org/10.1016/j.celrep.2014.03.001
68. Makeyev, A. V. & Liebhaber, S. A. The poly(C)-binding proteins: a multiplicity of functions and a search for mechanisms. RNA 8, 265-278 (2002). https://doi.org/10.1017/s1355838202024627
69. Lee, J. A. et al. Cytoplasmic Rbfox1 Regulates the Expression of Synaptic and Autism-Related Genes. Neuron 89, 113-128 (2016). https://doi.org/10.1016/j.neuron.2015.11.025
70. Ray, D. et al. A compendium of RNA-binding motifs for decoding gene regulation. Nature 499, 172-177 (2013). https://doi.org/10.1038/nature12311
71. Mendonsa, S. et al. Massively parallel identification of mRNA localization elements in primary cortical neurons. Nature Neuroscience 26, 394-405 (2023). https://doi.org/10.1038/s41593-022-01243-x
72. Love, M. I., Huber, W. & Anders, S. Moderated estimation of fold change and dispersion for RNA-seq data with DESeq2. Genome Biol 15, 550 (2014). https://doi.org/10.1186/s13059-014-0550-8
73. Kislauskis, E. H., Zhu, X. & Singer, R. H. Sequences responsible for intracellular localization of beta-actin messenger RNA also affect cell phenotype. J Cell Biol 127, 441-451 (1994). https://doi.org/10.1083/jcb.127.2.441
74. Cremer, H., Chazal, G., Goridis, C. & Represa, A. NCAM is essential for axonal growth and fasciculation in the hippocampus. Mol Cell Neurosci 8, 323-335 (1997). https://doi.org/10.1006/mcne.1996.0588
75. Wu, K. Y. et al. Local translation of RhoA regulates growth cone collapse. Nature 436, 1020-1024 (2005). https://doi.org/10.1038/nature03885
76. Penna, E. et al. Cystatin B Involvement in Synapse Physiology of Rodent Brains and Human Cerebral Organoids. Front Mol Neurosci 12, 195 (2019). https://doi.org/10.3389/fnmol.2019.00195
77. Ji, S. J. & Jaffrey, S. R. Intra-axonal translation of SMAD1/5/8 mediates retrograde regulation of trigeminal ganglia subtype specification. Neuron 74, 95-107 (2012). https://doi.org/10.1016/j.neuron.2012.02.022
78. Habib, K., Bishayee, K., Kang, J., Sadra, A. & Huh, S. O. RNA Binding Protein Rbms1 Enables Neuronal Differentiation and Radial Migration during Neocortical Development by Binding and Stabilizing the RNA Message for Efr3a. Mol Cells 45, 588-602 (2022). https://doi.org/10.14348/molcells.2022.0044
79. Chen, C.-Y. et al. AU Binding Proteins Recruit the Exosome to Degrade ARE-Containing mRNAs. Cell 107, 451-464 (2001). https://doi.org/10.1016/S0092-8674(01)00578-5
80. Sandler, H., Kreth, J., Timmers, H. T. & Stoecklin, G. Not1 mediates recruitment of the deadenylase Caf1 to mRNAs targeted for degradation by tristetraprolin. Nucleic Acids Res 39, 4373-4386 (2011). https://doi.org/10.1093/nar/gkr011
81. Chekulaeva, M. Mechanistic insights into the basis of widespread RNA localization. Nat Cell Biol 26, 1037-1046 (2024). https://doi.org/10.1038/s41556-024-01444-5
82. Weber, A. I. et al. Srsf1 and Elavl1 act antagonistically on neuronal fate choice in the developing neocortex by controlling TrkC receptor isoform expression. Nucleic Acids Res 51, 10218-10237 (2023). https://doi.org/10.1093/nar/gkad703
83. Cioni, J.-M. et al. Late Endosomes Act as mRNA Translation Platforms and Sustain Mitochondria in Axons. Cell 176, 56-72.e15 (2019). https://doi.org/https://doi.org/10.1016/j.cell.2018.11.030
84. Neves, S. R., Ram, P. T. & Iyengar, R. G protein pathways. Science 296, 1636-1639 (2002). https://doi.org/10.1126/science.1071550
85. Mita, S. et al. Transcallosal Projections Require Glycoprotein M6-Dependent Neurite Growth and Guidance. Cereb Cortex 25, 4111-4125 (2015). https://doi.org/10.1093/cercor/bhu129
86. Litterman, A. J. et al. A massively parallel 3' UTR reporter assay reveals relationships between nucleotide content, sequence conservation, and mRNA destabilization. Genome Res 29, 896-906 (2019). https://doi.org/10.1101/gr.242552.118
87. Damianov, A. et al. Rbfox Proteins Regulate Splicing as Part of a Large Multiprotein Complex LASR. Cell 165, 606-619 (2016). https://doi.org/10.1016/j.cell.2016.03.040
88. Singha, M. K. et al. An Optimized Enzyme-Nucleobase Pair Enables In Vivo RNA Metabolic Labeling with Improved Cell-Specificity. Biochemistry 61, 2638-2642 (2022). https://doi.org/10.1021/acs.biochem.2c00559
89. Baccanari, D. P., Davis, S. T., Knick, V. C. & Spector, T. 5-Ethynyluracil (776C85): a potent modulator of the pharmacokinetics and antitumor efficacy of 5-fluorouracil. Proc Natl Acad Sci U S A 90, 11064-11068 (1993). https://doi.org/10.1073/pnas.90.23.11064
90. Saito, T. & Nakatsuji, N. Efficient gene transfer into the embryonic mouse brain using in vivo electroporation. Dev Biol 240, 237-246 (2001). https://doi.org/10.1006/dbio.2001.0439
91. Catapano, L. A., Arnold, M. W., Perez, F. A. & Macklis, J. D. Specific neurotrophic factors support the survival of cortical projection neurons at distinct stages of development. J Neurosci 21, 8863-8872 (2001). https://doi.org/10.1523/jneurosci.21-22-08863.2001
92. Ameres, S., Herzog, V. A., Reichholf, B. et al. . Thiol-linked alkylation for the metabolic sequencing of RNA (SLAMseq). Protocol Exchange (2017).
93. Cunningham, F. et al. Ensembl 2022. Nucleic Acids Research 50, D988-D995 (2022). https://doi.org/10.1093/nar/gkab1049
94. Sedlazeck, F. J., Rescheneder, P. & von Haeseler, A. NextGenMap: fast and accurate read mapping in highly polymorphic genomes. Bioinformatics 29, 2790-2791 (2013). https://doi.org/10.1093/bioinformatics/btt468
95. Koboldt, D. C. et al. VarScan 2: somatic mutation and copy number alteration discovery in cancer by exome sequencing. Genome Res 22, 568-576 (2012). https://doi.org/10.1101/gr.129684.111
96. Trotta, E. On the Normalization of the Minimum Free Energy of RNAs by Sequence Length. PLOS ONE 9, e113380 (2014). https://doi.org/10.1371/journal.pone.0113380
97. Krismer, K. et al. Transite: A Computational Motif-Based Analysis Platform That Identifies RNA-Binding Proteins Modulating Changes in Gene Expression. Cell Rep 32, 108064 (2020). https://doi.org/10.1016/j.celrep.2020.108064
98. Grant, C. E., Bailey, T. L. & Noble, W. S. FIMO: scanning for occurrences of a given motif. Bioinformatics 27, 1017-1018 (2011). https://doi.org/10.1093/bioinformatics/btr064
99. Pollard, K. S., Hubisz, M. J., Rosenbloom, K. R. & Siepel, A. Detection of nonneutral substitution rates on mammalian phylogenies. Genome Res 20, 110-121 (2010). https://doi.org/10.1101/gr.097857.109
100. Kent, W. J., Zweig, A. S., Barber, G., Hinrichs, A. S. & Karolchik, D. BigWig and BigBed: enabling browsing of large distributed datasets. Bioinformatics 26, 2204-2207 (2010). https://doi.org/10.1093/bioinformatics/btq3511.

Acknowledgements

This work was supported by NIH Pioneer Award DP1 NS106665; Allen Distinguished Investigator Award ADI 11855 to J.D.M. from the Paul G. Allen Frontiers Group; and the Max and Anne Wien Professor of Life Sciences fund; with additional infrastructure support from NIH grants NS045523 and NS104055. P.V. was partially supported by NSF GRFP 280932, The NSF-Simons Center for Mathematical and Statistical Analysis of Biology at Harvard #1764269, and NIH Training Grant T32 GM007306-43. D.E.T. was partially supported by NIH F31 NS127518 and The NSF-Simons Center for Mathematical and Statistical Analysis of Biology at Harvard #1764269. We thank Joyce LaVecchio and Nema Kheradmand of the HSCRB-HSCI Flow Cytometry Core; the Bauer RNA sequencing core and the Harvard Center for Biological Imaging for infrastructure and support; Tim Sackton for statistical advice; and other members of the Macklis lab for helpful suggestions.

Author contributions

J.D.M. and P.V. conceived of the project; J.D.M., P.V., and D.E.T. designed experiments; P.V. and M.R. generated constructs; P.V. performed all mouse work. P.V. and D.E.T. performed soma preps and sorts; P.V. and D.E.T. performed library preparation for RNA sequencing; D.E.T. performed western blot validation; P.V. performed histology; P.V. performed bioinformatic analysis with input from D.E.T; P.V., D.E.T., and J.D.M interpreted data and wrote the manuscript. All authors read and approved the manuscript.

Competing interest statement

The authors declare no competing interests.

Materials and Methods

Mice

Experiments involving mice were performed with approval of the Harvard University Institutional Animal Care and Use Committee (IACUC) and in accordance with all federal and state guidelines. All data on callosal projection neurons (CPN) were collected from wild-type CD1 (Charles River Laboratories; RRID:IMSR_CRL:022) mouse pups of both sexes via subtype-specific expression of fluorescent proteins using unilateral *in*

utero electroporation (IUE) at embryonic day E14.5, targeting CPN in cortical layers II/III. Due to the exploratory nature of the investigations described here, a formal power analysis was not required or performed.

In utero electroporation

Subtype-specific labeling of CPN was achieved using unilateral *in utero* electroporation of genetic constructs at E14.5, as we and others have previously described[90]. Briefly, a pregnant female was anesthetized using 1.5-2% isoflurane, then prepared for surgery by applying eye ointment (#2444062, Systane), and administering buprenorphine (#60969, Par Pharmaceutical). Lower abdominal hair was removed using hair removal cream, and skin was locally disinfected with ethanol. An incision was made through skin and abdominal musculature, and the uterine horns were exposed, gently externalized from the intraperitoneal cavity onto a sterile gauze pad on the abdomen, where they were continuously kept moist using sterile, pre-warmed PBS. Embryos were individually positioned and injected unilaterally into a lateral ventricle with 0.7-1 ul DNA (5 ug/ul) supplemented with Fastgreen (#AAA16520-06, Thermo Scientific Chemicals) for visualization, using a pulled and beveled glass micropipette (#22-260-943, Fisher). DNA was electroporated into neural progenitors lining the ventricles by applying voltage across the injected cortical area (5 pulses, 50 ms on, 950 ms off, 34 V), targeting lateral sensorimotor areas of the cortical plate. Following electroporation, embryos were gently placed back into the intraperitoneal cavity, and the wound was closed using sutures (#39010, Covetrus). The pregnant dam was allowed to fully recover from anesthesia and surgery on a thermally-controlled mat under a low-intensity heat lamp before being returned to animal husbandry. Postoperative care following surgery included daily checks of overall well-being and the wound, and administration of buprenorphine (#60969, Par Pharmaceutical) every 12 hours for the first 3 days post-surgery. After birth, pups were screened for unilateral cortical fluorescence using a fluorescence stereoscope, and successfully electroporated pups were marked with a tail clip and included in downstream experiments, while unsuccessfully electroporated pups were excluded from downstream experiments - Attrition rate of electroporation was approximately 30% across all experiments.

DNA constructs

Constructs were derived from pCAG-[MCS]-IRES-GFP (CBIG), courtesy of C. Lois. For metabolic labeling, TdTomato (RRID:Addgene_26771) and UPRT (RRID:Addgene_47110) were cloned downstream of pCAG to create pCAG-myr-TdTomato and pCAG-myr-TdTomato-2A-UPRT. For *in vivo* luciferase library experiments, mClover (RRID:Addgene_74236) and luciferase (RRID:Addgene_38235) were cloned downstream of pCAG to create pCAG-mClover and pCAG-luciferase. Luciferase was then fused downstream of distinct 3' UTRs via InFusion cloning of custom primers (Azenta Life Science). All constructs were prepared using the Endotoxin-free Maxiprep kit (Qiagen, #12362), following manufacturer's instructions, and quality was verified using restriction enzyme digests and Sanger sequencing (Azenta Life Science) prior to CPN labeling via E14.5 IUE.

4-thiouracil injection

P2 or P3 pups were cryoanesthetized on ice for 60 seconds each, then 4-thiouracil (Sigma) was diluted in DMSO to 400 mg/kg, and injected subcutaneously into fat pads on back of neck, or into the intraperitoneal cavity, using a 30cc insulin syringe. Pups fully recovered on a thermal mat.

Doxycycline injection

P2 or P3 pups were cryoanesthetized on ice for 60 seconds each, then 20 ul (10 mg/uL) of doxycycline diluted in DMSO was injected into intraperitoneal cavity via Hamilton syringe. Pups fully recovered on a thermal mat

Subtype-specific soma isolation and purification via FACS

All metabolic labeling experiments were performed under red light. Soma isolation and subtype-specific purification via FACS were performed as we and others have previously described (https://doi.org/10.1038/s41596-021-00638-7)[24,91]. Briefly, P3 pups, which had been electroporated at E14.5 to label CPN, were deeply anesthetized in ice and decapitated, enabling brain extraction from the skull. Fluorescently labeled neurons in layer II/III were microdissected in ice-cold HBSS (Thermo 14025134) via a fluorescence stereomicroscope, and transferred to a Falcon tube with dissociation solution (DS). Microdissected cortical tissue containing CPN from 2-3 pups was used for each sample. Tissue was washed twice with 3-5 mL DS, then enzymatically dissociated by incubating twice with 5 mL enzyme solution (ES) supplemented with DNaseI for 15 min per incubation. ES was removed, and tissue was washed twice with wash solution (WS), then mechanically dissociated via gentle trituration with a fire polished glass Pasteur pipet. Dissociated CPN were washed in 10 mL WS and pelleted at 80*g* for 5 min at 4 °C. Supernatant was removed, and neurons were resuspended in 500 ul WS using a fire polished glass Pasteur pipet. Subtype-specific, labeled CPN were sorted into RLT buffer (Qiagen) supplemented with 10% beta mercaptoethanol (Thermo 31350010) by blinded machine operators using a customized SORP FACSAriaII (BD Instruments) equipped with a 300 MW 488 nm laser set to 100 MW with large beam height, and an 85 um nozzle run at 45 psi, with the UV laser turned off, to prevent potential metabolic labeling interference.

Axon microdissection

All metabolic labeling experiments were performed under red light. P3 pups, which had been electroporated at E14.5 to label CPN, were deeply anesthetized in ice and decapitated, enabling brain extraction from the skull. Fluorescent axons from somata in layer II/III were microdissected from the corpus callosum in ice-cold HBSS (Thermo 14025134) using a fluorescence stereomicroscope. "Proximal axons" were dissected from the ipsilateral hemisphere using both a lateral boundary to avoid the electroporated somata and a medial boundary located 2 mm from the midline. "Distal axons" were dissected from the contralateral hemisphere from 2 mm from the midline to the edges of visible fluorescence. Microdissected regions from 2 pups were used for each sample. Axon segments were placed in 350 uL RLT (Qiagen AllPrep Kit) supplemented with beta mercaptoethanol (Thermo 31350010). Tissue was homogenized with a 26G needle and syringe prior to RNA isolation.

RNA isolation

For metabolic labeling experiments, RNA was isolated via a Qiagen AllPrep Kit, according to manufacturer's instructions, using RNeasy MinElute columns and the following modifications: buffer RPE was supplemented with beta mercaptoethanol (Thermo 31350010) to a final concentration of 10 mM, and RNA was eluted in 1 mM DTT (Thermo P2325). For metabolically labeled axon samples, protein was extracted from the initial flow-through, according to manufacturer's instructions, solubilized in 5% SDS, and quantified using the Qubit broad range protein assay for downstream normalization analysis. RNA was carboxyamidomethylated in a 50 ul reaction, as previously described[92] (50% DMSO (Sigma 41640), 10mM iodoacetamide (Sigma I1149), 50mM sodium phosphate buffer pH 8.0 (Sigma 74092 and 94046), and 1x Superase RNase Inhibitor (Invitrogen AM2696)) at 50 °C for 15 min, then quenched with 1 ul of 1 M DTT (Thermo P2325). RNA cleanup was performed with Zymo Clean and Concentrator-5. RNA was eluted in 10 ul water, and samples were stored at -80 °C. Otherwise, RNA was isolated via a Qiagen AllPrep Kit using RNeasy MinElute columns. RNA quality was assessed on a Tapestation 2100 with the High Sensitivity RNA kit (Agilent) prior to library preparation and RNA sequencing.

Library preparation and RNA sequencing

For metabolically labeled somata, the QuantSeq FWD kit with hexamer UMIs (Lexogen) was used for library preparation, using ~20-100 ng RNA per sample, then a NovaSeq (Ilumina) was used for 100 bp single-end reads via 3' end sequencing for ~25-40M reads per sample. For axons, libraries were prepared with SmartSeq v4 (Takara Bio) ¼-volume reactions, using ~5 ng RNA per sample, then a NovaSeq (Ilumina) was used for 2x150 bp paired-end reads via full-transcript sequencing (increasing coverage and detection of T->C conversions) for ~25-40M reads per sample. For luciferase library experiments, RNA was reverse transcribed with oligo-dT primers and the SuperScript IV First-Strand Synthesis System (Invitrogen 18091050), then primers with overhangs compatible with distinct 3' UTRs and Ilumina indexing primers were used to amplify desired mRNA regions. qPCR was performed with Lexogen PCR Add-on and Reamplification Kit V2 (Lexogen 208.96) to determine optimal cycle numbers, then indices were added with Lexogen UDI 12 nt Unique Dual Indexing V2 Add-on Kit B1 (Lexogen 202.96). A NextSeq (Ilumina) was used for 2x50 bp paired-end reads via full-transcript sequencing for ~4M reads per sample.

Perfusion, tissue processing, and immunocytochemistry

Postnatal mice were deeply anesthetized in ice and transcardially perfused with 3-5 mL of ice cold PBS, followed by 5 mL of cold 4% paraformaldehyde (PFA). Brains were extracted from the skull, and postfixed in 4% PFA overnight. The next day, perfused brains were washed in PBS, and cryoprotected with 30% sucrose in PBS. Tissue was embedded in O.C.T. (#25608-930, Sakura Finetek USA Inc), sectioned via cryostat (Leica, 50 um coronal sections), and collected in PBS with 0.025% azide. For immunocytochemical labeling, tissue was blocked in PBS with 0.3% TritonX100, 0.3% BSA, and 2% donkey serum for 1 hour at room temperature, then incubated with primary antibodies (RFP #600-401-379 Rockland; HA #H3663 Sigma) in blocking buffer on a rocker overnight at 4 °C. The next day, sections were washed 3 times in PBS on an orbital shaker, incubated for 2-3 hours at room temperature with fluorescently-conjugated secondary antibodies (Life Technologies) and DAPI (1:10,000,

#D1306 Thermo), washed 3 times with PBS, mounted on glass slides (Superfrost, #48311-702 VWR), coverslipped with fluoromount (#0100-01 VWR/Southern Biotech), and sealed with nail polish. Images were acquired via an epifluorescence microscope with a motorized stage and a 10x objective (Nikon NiE). Whole sections were imaged via EDF z-stack projections and mosaic image stitching with NIS Elements (Nikon).

Sequence alignment and conversion calling

Sequences were aligned to GRCm38[93] via Next-Gen Map[94] with the "-slam" option to account for T->C nucleotide conversions. SNPs were called for each sample, using samtools mpileup (RRID:SCR_002105) and VarScan2[95], and all high-quality variants were pooled to generate a reference for SNPs in our CD1 mouse strain (RRID:IMSR_CRL:022). Custom scripts, publicly available on GitHub, were used to detect conversions in the read sequence compared to the reference while masking SNPs.

Estimating new transcript ratios

NTR was estimated as others have previously described[40], with some slight modifications. Briefly, the conversion error rate (p_{old}) was calculated as the sample conversion rate of unlabeled samples. In each labeled sample, the likelihood of observing a certain number of T->C conversions in a read was parameterized by a Poisson mixture model:

TC_i: number of T->C conversions in read "i"
T_i: number of Ts observed in read "i"
θ: NTR for a gene "g" in sample "s" ($\theta_{g,s}$), or for a sample "s" (θ_s)
$p_{new,s}$: probability of a T->C conversion in new RNA for a sample "s"
p_{old}: probability of a T->C conversion in old RNA (errors)

$$f(TC_i|\theta, p_{new}, p_{old}, T_i) = \theta * f(TC_i|p_{new}, T_i) + (1-\theta) * f(TC_i|p_{old}, T_i)$$
$$f(TC_i|p, T_i) \sim Poisson(p * T_i)$$

For sample-wide estimates, the maximum likelihood estimates for $p_{new,s}$ and for θ_s were obtained. The $p_{new,s}$ was then used to calculate maximum likelihood estimates for $\theta_{g,s}$ for each gene in every sample

Estimating half-lives

Relative half-lives were determined as follows:

θ: new transcript rate (NTR)
$y(t)$: mRNA levels at time "t"
p: production of mRNA (constant in t)
k: degradation/loss of RNA

θ estimates follow from the equation describing steady-state mRNA levels:

$\frac{\partial y}{\partial t} = p - ky(t)$; change in y is a first-order differential equation
$y(t) = \left(y_0 - \frac{p}{k}\right) e^{-kt} + \frac{p}{k}$; closed form solution from time 0 to t
$y_{new}(t) = -\frac{p}{k} e^{-kt} + \frac{p}{k}$; find y_{new} by setting $y_0 = 0$ at t = 0
$\frac{\partial y}{\partial t} = 0 \rightarrow y_{ss} = \frac{p}{k}$; determine y a steady state
$y_{old}(t) = y_{ss} - y_{new} = \frac{p}{k} e^{-kt}$; find y_{old} by subtracting y_{new} from y_{ss}
$\theta = \frac{y_{new}}{y_{new} + y_{old}} = 1 - e^{-kt}$; new transcript proportion is a f(t, k)
$1 - \theta = e^{-kt}$; old transcript proportion is a f(t, k)

The estimate for half-life (t_h) then follows:

$\frac{1-1/2}{1-0} = \frac{e^{-kt_h}}{e^{-k*0}}$; half of the old RNA remains when θ = 1/2
$1/2 = e^{-kt_h}$; simplify
$\frac{ln\,(2)}{k} = t_h$; solve for t_h

Identification of labeled transcripts in axons

Since axonal transcripts are expected to be mature mRNAs, we accounted for variability across mouse 4TU injections by normalizing conversions per gene based on the median intron conversion rate across each sample (Figures S4E-F). We set a gene detection threshold of > 50 reads and > 1.5 normalized conversions per 1,000 Ts, which was required in >2/3 of samples of a particular sample type to include that gene for additional downstream analyses (Figure S4G). A negative binomial adaptation of a GLM was then fit to these data (using glm.nb from the MASS package in R). The default log link function was used for the response variable $TC_{scale:g,s}$, which we defined as follows:

$TC_{scale:g,s} = TC_g * \gamma_s * \tau_{g,s}$: T->C conversions observed (TC_g) scaled by an intron labeling factor (γ_s) and a T-scaling factor ($\tau_{g,s}$)

$$\gamma_s = \frac{median}{j\ in\ samples}(\gamma_j)/\gamma_s$$
$$\tau_{g,s} = \frac{median}{j\ in\ samples}(T_{g,j})/T_{g,s}$$

And the linear term is:

$TC_{scale:g,s} \sim \beta_0 + \beta_{UPRT} * I_{UPRT} + \varepsilon$; Intercept ($\beta_0$) modified by UPRT coefficient (β_{UPRT}), whether sample contains UPRT (I_{UPRT}), and error (ε)

The model was first fit with all data, then (1) with "leave-one-out" cross validation (remove 1 sample in each training run, then assess model performance on the held-out sample), and (2) with "bootstrapping" (randomization of group assignments to simulate a null distribution of β_{UPRT} estimates). Significance was assessed using a one-sided Wald test for β_{UPRT} coefficient, and p-values were corrected via Benjamini-Hochberg procedure.

RNA features analysis

UTR Sequences: QuantSeq soma reads were aligned to GRCm38. To define associations between 3' UTRs and observed reads, a pileup of 5' ends was generated, then intersected with 3' UTRs from Ensembl version 101 (RRID:SCR_002344). If a pileup was within 250bp of a 3' end, it was assigned to that 3' UTR isoform. If a pileup was further from a 3' end (typically > 500bp), a new "truncated" 3' end isoform was called. 3' UTR sequences were retrieved from Ensembl bioMart, and "truncated" isoform sequences were generated as a substring of annotated parent 3' UTRs. These UTR sequences were applied to axons.

Normalized minimum free energy of folding (MFE): All sequences were run through Vienna RNAFold with standard paramaters to calculate MFE. Simulated background sequences were randomly generated with varying %GC content (20-80%) and length (50-10,000 bp). Each "true" sequence was binned by %GC content and length, and the respective background was used to calculate normalized MFE, as previously described[95]: $100*(MFE_{observed}-MFE_{simulated})/(L-L_0)$; $L_0 = 8$.

AU-rich element (ARE) score: For each sequence, ARE scores were calculated as previously described[65]. For Figure 2D, whole 3' UTR sequences were used to calculate ARE scores without length normalization. For Figure S2C, ARE scores were computed using 50 bp windows to enable comparisons between all 3' UTR regions and all AU repeat centered regions.

Motif enrichment: Enrichment for RBP motifs was computed using the Transite program and R package[97], which employs a hypergeometric test to compare motif prevalence in a subset relative to background.

Motif scanning: FIMO[98] from the MEME suite was used to scan sequences for particular motifs. Standard parameters were used.

Evolutionary Conservation Analysis: phyloP[99] scores for placental mammals were obtained from the UCSC Genome Browser (RRID:SCR_005780), and average scores across a 50 bp genomic window were computed using bigWigAverageOverBed[100]. Windows were centered on AU repeats, or tiled across entire 3' UTRs with 10 bp steps.

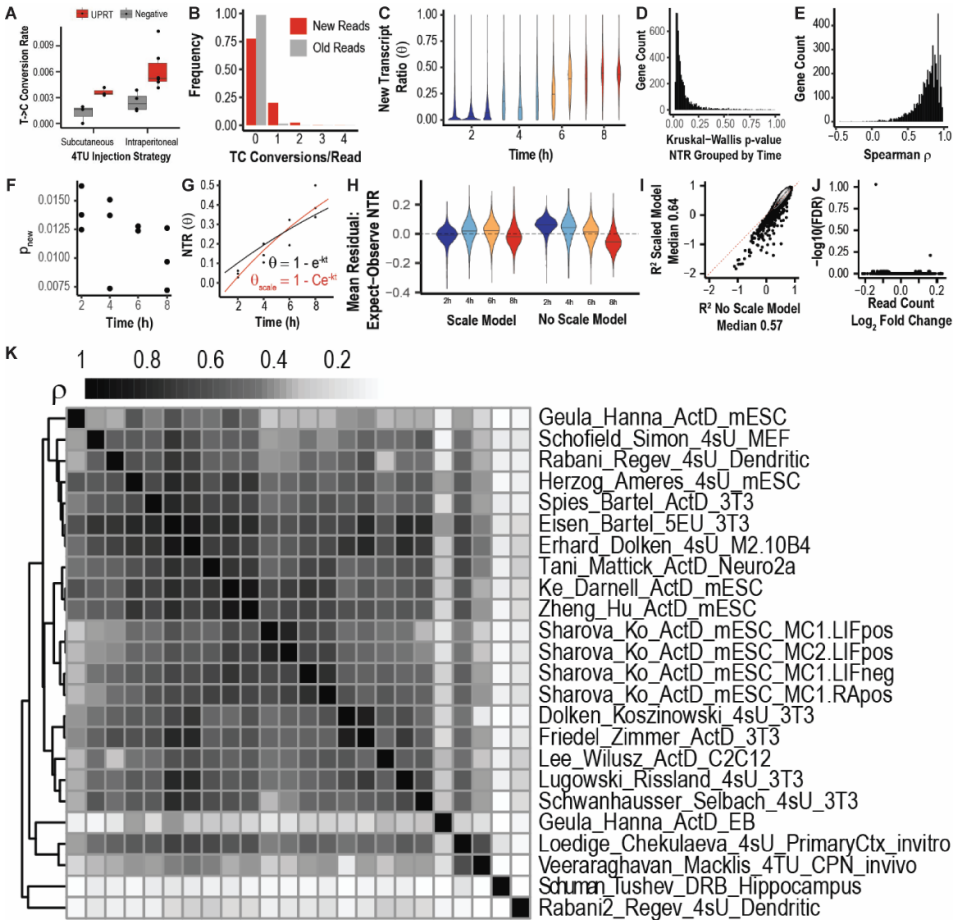

Figure S1: Identification of CPN transcript half-lives via *in vivo* metabolic labeling. (A) Intraperitoneal injection of 4-thiouracil (4TU) leads to more significant incorporation over background. **(B)** New reads are more likely to have T->C conversions (true label) than old reads (background label). **(C)** Genome-wide, per-sample new transcript ratio (NTR) estimates increase after 4TU injection. **(D)** Per-gene comparisons of NTR within a timepoint group versus between timepoint groups identifies that most variability arises from differences between timepoints, rather than from within timepoints. **(E)** Per-gene Spearman correlation coefficient between NTR and time identifies that NTR increases over time. **(F)** Probability of T->C conversions in new RNA (p_{new}) decreases over time, consistent with 4TU clearance. **(G)** Estimating k_{deg} to calculate RH_{soma} ($\ln(2)/k_{deg}$) with (red) or without (black) a scalar to account for 4TU clearance. **(H)** Residuals for the "scaled" model do not negatively correlate with time, unlike residuals for the "unscaled" model. **(I)** The "scaled" model has slightly better R^2 goodness of fit compared to the "unscaled" model. **(J)** No mRNAs change significantly over time ($q < 0.05$), validating mRNA steady-state assumptions. **(K)** Among all studies, RH_{soma} Spearman correlation is best with half-lives from primary cultured cortical neurons.

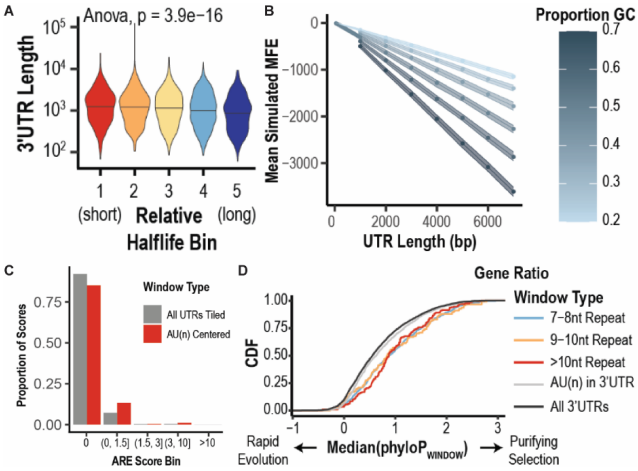

Figure S2: *Cis*-regulatory features are associated with *in vivo* CPN transcript half-lives. (A) 3' UTR length negatively correlates with CPN soma mRNA half-life (RH_{soma}). **(B)** Simulated background scores for minimum free energy of folding (MFE) vary by %GC content and 3' UTR length. **(C)** Most AU repeats do not overlap with AU-rich element (ARE) motifs across 50 bp windows. **(D)** Per-gene AU repeats in 3' UTRs have more evolutionary conservation.

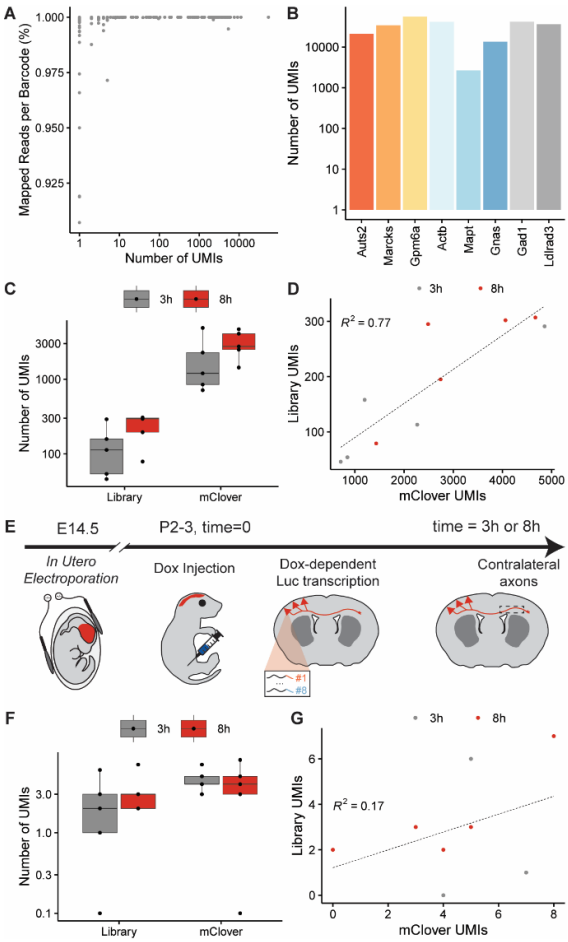

Figure S3: Identification of 3' UTR barcodes from luciferase library in somata, but not axons. (A) All 3' UTR barcodes are identified confidently by unique molecular identifiers (UMIs). **(B)** All 3' UTR barcodes are identified at high abundances, as quantified by number of UMIs per 3' UTR barcode. **(C)** UMIs for barcodes and mClover increase over time after doxycycline injection, motivating normalization by library and mClover abundances. **(D)** UMIs for barcodes and mClover are well-correlated, enabling use of both factors for normalization. **(E)** Schematic for *in vivo* inducible luciferase library assay in CPN axons. CPN express fluorophore and a library of doxycycline-dependent luciferases, each of which is fused to a distinct 3' UTR, via E14.5 IUE. At P2 or P3 (t = 0), doxycycline is administered via intraperitoneal injection, then fluorescent CPN axons are isolated at distinct time points via microdissection for RNA extraction, sequencing, and differential expression analysis. **(F)** UMIs for barcodes and mClover are not abundant in CPN axon samples, likely due to the limited level of enrichment. **(G)** UMIs for barcodes and mClover are poorly correlated, due to low abundance of these mRNAs in CPN axons.

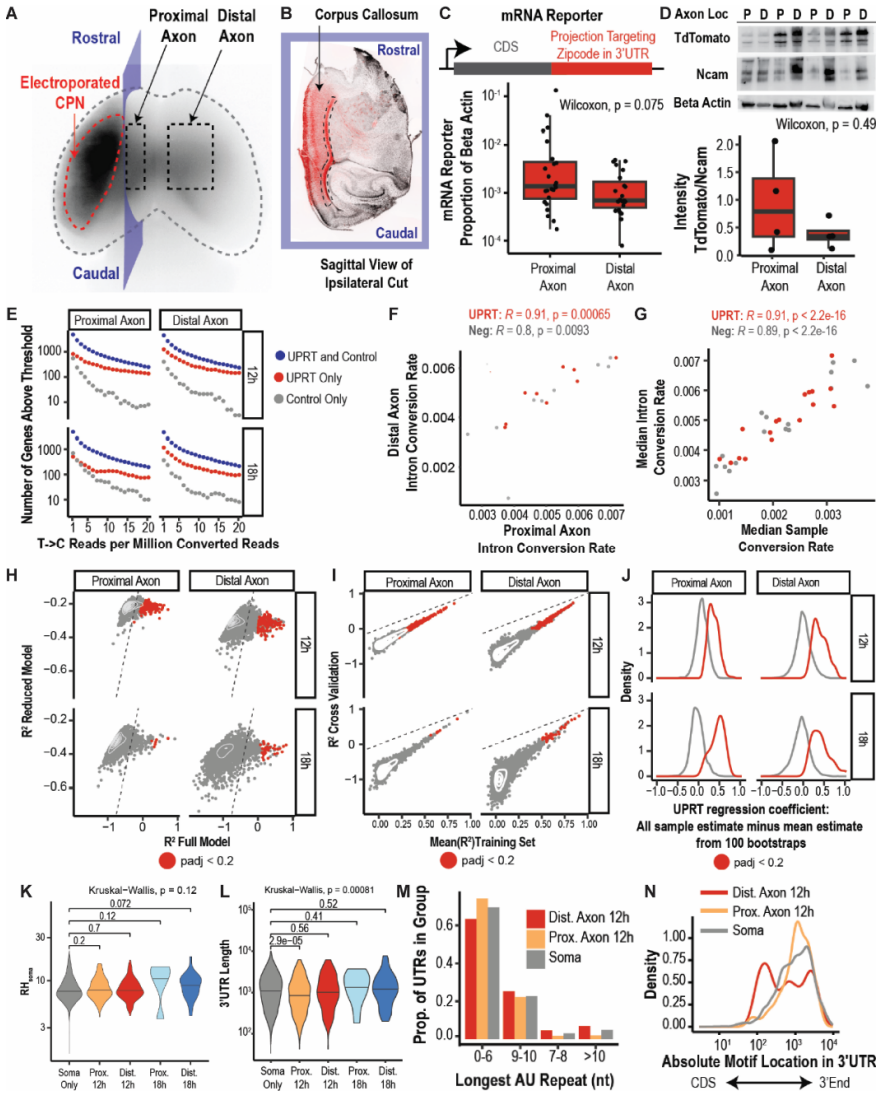

Figure S4: Identification of mRNAs in CPN axons via *in vivo* metabolic labeling. (A) CPN labeled via E14.5 IUE extend axons to contralateral cortex, as demonstrated by whole-mount imaging. **(B)** CPN axons are fluorescently microdissected, shown in the parasagittal section of the labeled brain from (A). **(C)** mRNA reporter is significantly more abundant in proximal axons (relative to beta actin), as identified by qPCR. **(D)** TdTomato appears non-significantly more abundant in proximal axons (relative to Ncam), as identified by western blot. **(E)** UPRT samples have more mRNAs above T->C conversion thresholds in ¾ of samples than non-UPRT samples. **(F)** Median intron conversion rates are well correlated between proximal and distal axons, enabling normalization. **(G)** Median intron conversion rates are well correlated with median T->C conversion rates, enabling normalization. **(H)** A negative binomial generalized linear model (GLM) performs better with a β_{UPRT} term ("full" model) than without it ("reduced" model) for some mRNAs, enabling identification of axon mRNAs. R^2 measures "goodness of fit". **(I)** R^2 between "training" (one held-out sample) and cross-validation (containing the held-out sample) is positively correlated across training runs, suggesting that this model is generalizable. **(J)** "True" value of β_{UPRT} (full model – mean(bootstrapped β_{UPRT})) is strongly positive for labeled mRNAs in axons. **(K)** RH_{soma} does not change significantly across axon samples, but appears non-significantly higher in 18 hour axons. **(L)** 3' UTR lengths change significantly across axon samples, and are significantly lower in proximal, 12 hour axons. **(M)** mRNAs in distal, 12 hour axons have longer AU repeat motifs in their 3' UTRs. **(N)** AU repeats in mRNAs from distal, 12 hour axons are closer to coding sequences (CDS).